Paramagnetic Phases of Strongly Correlated Ultracold Fermions Coupled to an Optical Cavity

Renan da Silva Souza,* Youjiang Xu, and Walter Hofstetter[†]
Goethe-Universität, Institut für Theoretische Physik, 60438 Frankfurt am Main, Germany
(Dated: November 17, 2025)

We numerically study a gas of two-component fermions coupled to a transversely pumped optical cavity and confined to a two-dimensional static square optical lattice. In the dispersive regime, the steady state of the system is described by an extended Hubbard Hamiltonian with cavity-mediated long-range interactions. Using real-space dynamical mean-field theory (RDMFT), we investigate the formation of the (superradiant) checkerboard density-wave phase both at quarter and half filling. We focus on the paramagnetic phase assuming sufficiently high temperatures such that no magnetic long-range order develops. At quarter filling, we find a reentrant homogeneous Fermi liquid to density wave phase transition with increasing temperature, which is due to the higher entropy of the ordered phase. At half filling, in addition to the Fermi liquid to Mott insulator phase transition, marked by a vanishing quasiparticle residue at the Fermi level, we identify the transition into a density-wave phase. Due to perfect Fermi surface nesting at half filling, we find that arbitrarily small long-range interactions destabilize the system towards the density-wave phase in the absence of short-range interactions. By varying short- and long-range interactions at a fixed low temperature, we obtain the full phase diagram and identify a region of coexistence between the homogeneous Fermi liquid and Mott insulating phase with the density-wave phase. In this region, we determine the thermodynamic phase transition by comparing the energies of the different RDMFT solutions.

I. INTRODUCTION

Understanding the effect of non-local interactions in strongly correlated quantum many-body systems is a long-standing question in physics. This question arises, for instance, when considering the long-range interactions of dipolar [1–4] and Rydberg-excited quantum gases [5–7] or the Coulomb interaction [8–35] between electrons in a metal. A unique approach to address this problem is to investigate a quantum gas coupled to a single-mode optical cavity driven by a pump laser [36]. In this setting, the two-photon processes between the cavity and the pump mediate an effective global long-range interaction among the atoms. This experimental setup has enabled the observation of the superradiant self-organization quantum phase transition, where a checkerboard density-wave pattern emerges in the atomic density simultaneously with steady-state superradiance marked by the macroscopic number of photons occupying the cavity mode which is caused by the coherent scattering of pump photons into the cavity. This phenomenon was first observed in a transversely-driven atomic Bose-Einstein condensate loaded into an optical cavity [37]. Since then, significant experimental progress has been made with bosons coupled to optical cavities, including the investigation of symmetry breaking across the transition [38], the measurement of the softening of the lowest-energy polariton mode [39], the observation of quench dynamics across the non-equilibrium phase transition [40], and the determination of the atomic dynamic structure factor from the power spectral density of the

cavity radiation field [41].

In recent experiments the effect of cavity-mediated long-range interactions on two-component spinful ultracold Fermi gases of ⁶Li atoms was studied [42–48]. The self-organization of the atomic density and associated superradiance was first realized for a non-interacting ultracold Fermi gas [45] and more recently for a unitary Fermi gas with attractive contact interactions due to swave scattering, where the scattering length was tuned across the BEC-BSC crossover [46]. One of the main novel features of the fermionic superradiance compared to its bosonic counterpart is its strong dependency on the atomic density. As demonstrated theoretically for spinless fermions without short-range interactions [49–51], the Fermi surface nesting effect, where one portion of the Fermi surface is mapped onto another by a single wave vector matching the cavity photon momentum, can significantly decrease the threshold for the emergence of atomic self-organization for certain fillings.

One possibility of investigating this effect in greater detail is to confine the system to a two-dimensional static square optical lattice. For sufficiently deep lattices and at low fillings, the atomic system can be described by a Fermi–Hubbard model [52]. In this setting, the Fermi surface of the two component Fermi gas exhibits perfect nesting [31]. Such a lattice further allows for tunable onsite Hubbard interactions between the two fermionic components.

For bosons coupled to an optical cavity, the competition between onsite and cavity-mediated long-range interactions has been studied within the extended Bose–Hubbard model [53–57], which has also been realized experimentally [58–60]. In particular, for single-component bosons in the strong-interaction regime, a region of metastability where Mott-insulating and density-

^{*} souza@itp.uni-frankfurt.de

[†] hofstett@physik.uni-frankfurt.de

wave phases coexist was predicted [56, 59] and later confirmed experimentally [60].

In the fermionic case, extended Hubbard models have been widely used to investigate strongly correlated electrons in solids, where the Coulomb interaction is only partially screened. The extended Hubbard model with nearest-neighbor interactions has been studied using a variety of techniques, including among others, Hartree-Fock mean-field [10, 11, 13, 19], coherent potential approximation [17], variational cluster approach [21], exact diagonalization [18, 22, 26], the two-particle self-consistent approach [23], Monte Carlo simulations [8, 9, 12], density-matrix renormalization group [14, 16], and dynamical mean-field theory (DMFT) [15, 20, 25, 27, 28, 34] and its extensions [24, 29–33, 35]. Of particular relevance to our study are the DMFT results of Refs. [15, 34]. In [15], the extended Hubbard model with nearest-neighbor interactions on a Bethe lattice was studied at quarter filling, where reentrant behavior was found: increasing temperature drives a transition from a homogeneous Fermi liquid to a density-wave phase. Later, [34] analyzed the same model at general filling and demonstrated that at half filling the system exhibits a region of metastability between Fermi-liquid, Mott-insulating, and density-wave solutions obtained within DMFT. The realization of cavity-mediated long-range interactions in ultracold Fermi gases coupled to an optical cavity opens up the possibility of observing similar physics in a different setting.

For a one-dimensional Fermi-Hubbard chain coupled to a transversely pumped cavity, exact diagonalization revealed that tuning the pump polarization allows stabilization of diverse phases, including density waves, antiferromagnetic insulators, pair superfluids, and pair density waves [61]. Recently, the same system was analyzed in Refs. [62, 63], where fluctuations beyond the mean-field atom-cavity coupling were included, revealing a regime of bistability in the superradiant, selforganized phase. Despite these advances, the interplay between cavity-mediated long-range interactions and onsite Hubbard repulsion in fermionic lattice systems remains largely unexplored. In particular, in the regime where both interactions are strong, it is an open question whether the transition between the Mott insulator and the density-wave insulator is of first order, as has been observed for bosonic systems with short-range and long-range cavity-mediated interactions [56, 60].

Motivated by these considerations, here we consider a two-component Fermi gas in a two-dimensional static square optical lattice. The Fermi gas is coupled dispersively to a single-mode optical cavity and pumped by a transverse coherent laser field (Fig. 1a)). Considering a sufficiently deep lattice, we derive an extended Hubbard model with cavity-mediated density-density long-range interactions to describe the system. We consider a balanced configuration, where we assume that the densities of the two fermionic components are equal and that no magnetic order emerges in the system. In

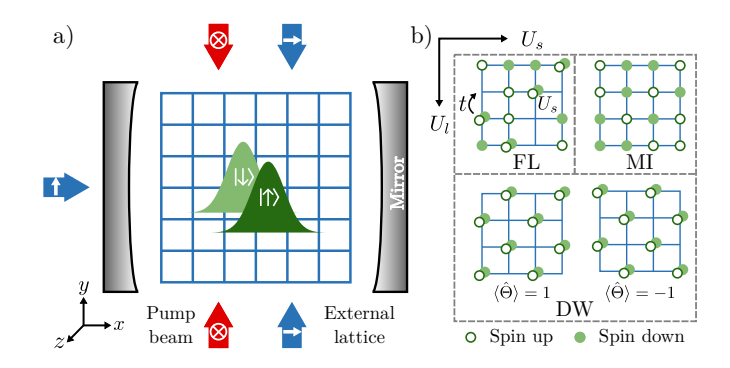


FIG. 1. a) Schematic representation of a two-component Fermi gas (with the two components (hyperfine states) denoted as $|\uparrow\rangle$, $|\downarrow\rangle$) confined to a static square optical lattice inside a single mode optical cavity. The atoms are transversely driven by a coherent pump-laser field. b) Schematic illustration of the atomic configuration of the different quantum phases we observe in the system at half filling. For weak long-range interactions U_l , we observe a phase transition from a Fermi-liquid phase (FL) to a Mott-insulating phase (MI) as the short-range interaction U_s is increased. For fixed U_s , increasing U_l drives the system into a density-wave insulating phase (DW), in which the atoms self-organize, occupying either the even or the odd sublattice. In this phase, the expectation value of the occupation imbalance operator $\langle \Theta \rangle$ (Eq. (7)) asymptotically approaches +1 for a checkerboard pattern with occupied even sites and -1 for occupied odd sites.

this setting, we find that the self-organized checker-board density-wave phase competes with homogeneous paramagnetic metallic (Fermi liquid) and Mott insulating phases (Fig. 1b)). The global range of the cavity-mediated interactions justifies their static mean-field decoupling, as demonstrated for bosonic systems coupled to a cavity in [64]. This approach has proven to be effective in characterizing the phase transitions in such systems [53–56]. Our analysis of the resulting problem is based on real-space Dynamical Mean-Field Theory (RDMFT) [65], which maps the full Hubbard model onto a set of effective single-impurity problems which are coupled via a self-consistency condition. This method allows us to characterize the phases of the system for different parameter values and to investigate the transitions between them.

We focus on the paramagnetic phases at quarter and half filling, assuming that the temperature is sufficiently high to suppress magnetic long-range order. In both cases, we observe the emergence of a checkerboard density-wave phase and study the effect of varying temperature on the phase diagram. At quarter filling, we observe that for fixed short- and long-range interactions increasing temperature can drive a reentrant transition from a metallic phase into the checkerboard density-wave phase, as also observed in previous DMFT calculations for the extended Hubbard model [15]. At half filling, we find that in the absence of short-range interactions, arbitrarily weak long-range interactions induce the checkerboard density-wave phase, as a consequence

of perfect Fermi-surface nesting [49–51]. For small but finite short-range interactions, increasing the long-range interaction strength triggers a metal to density-wave phase transition. Conversely, for weak long-range interactions and intermediate to strong short-range interactions, we observe a paramagnetic Mott transition captured by the vanishing of the quasiparticle residue at the Fermi level. For sufficiently strong short-range interactions a phase transition from a Mott insulator to a density-wave phase is found upon increasing the long-range interaction strength. For intermediate-to-strong short- and longrange interactions, we find regions of the phase diagram where the density-wave-ordered DMFT solution coexists with either the homogeneous Fermi-liquid or Mottinsulating solution. In these regions the DMFT solution exhibits a hysteresis loop: If for a fixed short-range interaction strength one starts from the Fermi-liquid phase or from the Mott-insulating phase and gradually increases the long-range interaction strength the transition to the density-wave phase will occur at a larger critical interaction strength than upon decreasing the interaction strength starting from the density-wave phase. This indicates the first-order nature of this transition and can be explained by analyzing the expectation value for the energy of the system in the limit of vanishing tunneling [56, 60] (see appendix A). In this region, we determine the thermodynamic phase transition by calculating and comparing the energy of the different DMFT solutions.

In the following, we derive the effective Hamiltonian in section II, then describe the RDMFT method in section III, and present and discuss our results in section IV. Final remarks are presented in section V.

II. FERMI-HUBBARD MODEL WITH LONG-RANGE INTERACTIONS

We consider a balanced two-component ultracold Fermi gas with contact interactions arising from s-wave scattering, coupled to a single-mode high-finesse optical cavity. The quantized cavity mode of frequency ω_c and wave number $k_c = k$ is λ -periodic along the xdirection. The Fermi gas is driven by a coherent pump laser of frequency ω_p and wave number $k_p \approx k$ along the y-axis. The system is confined to a two-dimensional layer of a cubic optical lattice, which is deep along the z-direction, and experiences a static square optical lattice potential with wave vector $k_{\text{latt}} = k$ and N_s sites in the xy-plane (see Fig. 1a)), similar to the experimental setting realized in [59]. The two components, denoted as $|\uparrow\rangle$ and $|\downarrow\rangle$, correspond to the two lowest hyperfine states of ⁶Li, as experimentally realized in [42, 45], where in the Paschen-Back regime, the transition $|2S_{1/2}, m_J = -1/2\rangle \to |2P_{3/2}, m_J = -3/2\rangle$ serves as a two-level system with resonant frequency ω_a for each

In the frame rotating with frequency ω_p , the effective Hamiltonian describing the system is $\hat{H}_A - \Delta_c \hat{a}^{\dagger} \hat{a}$, where

 \hat{a} is the bosonic cavity mode annihilation operator and $\Delta_c = \omega_p - \omega_c$ is the pump-cavity detuning. We separate the Hamiltonian describing the fermionic atoms into a noninteracting part \hat{H}_0 and a two-body interaction term $\hat{H}_{\rm int}$, i.e. $\hat{H}_{\rm A} = \hat{H}_0 + \hat{H}_{\rm int}$. If the atom-pump detuning $\Delta_a = \omega_p - \omega_a$ is large, the dynamics of the atomic excited state can be adiabatically eliminated [66, 67]. In this regime, the free-fermion Hamiltonian reads

$$\hat{H}_0 = \sum_{\sigma} \int d^3 x \hat{\Psi}_{\sigma}^{\dagger}(\boldsymbol{x}) \hat{h}_0 \hat{\Psi}_{\sigma}(\boldsymbol{x}), \qquad (1)$$

$$\hat{h}_0 = -\frac{\hbar^2}{2m} \nabla^2 + \hat{V}_{\text{eff}}(\boldsymbol{x}) - \mu_{\sigma}, \qquad (2)$$

where $\hat{\Psi}_{\sigma}(\boldsymbol{x})$ is the fermionic annihilation field operator of an atom in state $\sigma \in \{\uparrow, \downarrow\}$. The two fermionic components experience an effective potential

$$\hat{V}_{\text{eff}}(\boldsymbol{x}) = V_{\text{latt}}(\boldsymbol{x}) + \hbar [V(\boldsymbol{x}) + U(\boldsymbol{x})\hat{a}^{\dagger}\hat{a} + \eta(\boldsymbol{x})(\hat{a} + \hat{a}^{\dagger})], (3)$$

where $V_{\text{latt}}(x) = V_{2\text{D}}[\cos^2(kx) + \cos^2(ky)]$ is the external static square optical lattice with depth $V_{2\text{D}}$, $V(x) = V_0 \cos^2(ky)$ is the pump lattice with depth $\hbar V_0 = \hbar \Omega_0^2/\Delta_a$, where Ω_0 is the maximum Rabi frequency of the pump laser, $U(x) = U_0 \cos^2(kx)$ is the cavity potential with depth per photon $\hbar U_0 = \hbar \mathcal{G}_0^2/\Delta_a$, where \mathcal{G}_0 is the maximum coupling strength of the atom to the cavity, and finally $\eta(x) = \eta_0 \cos(kx) \cos(ky)$ is the checkerboard lattice generated by cavity-pump coupling with $\hbar \eta_0 = \hbar \Omega_0 \mathcal{G}_0/\Delta_a$ being the maximum two-photon Rabi frequency. Furthermore, the two-body interatomic interaction is described by the Hamiltonian

$$\hat{H}_{\rm int} = g \int d^3x \hat{\Psi}_{\uparrow}^{\dagger}(\boldsymbol{x}) \hat{\Psi}_{\downarrow}^{\dagger}(\boldsymbol{x}) \hat{\Psi}_{\downarrow}(\boldsymbol{x}) \hat{\Psi}_{\uparrow}(\boldsymbol{x}), \qquad (4)$$

where $g = 4\pi a_s \hbar^2/m$ with a_s being the s-wave scattering length.

When the static optical lattice $V_{\rm latt}$ is sufficiently deep, the atomic field operators can be expanded in terms of the lowest band Wannier functions as $\hat{\Psi}_{\sigma}(x) = \sum_{i} w_{i}(x)\hat{c}_{i\sigma}$, where $\hat{c}_{i\sigma}$ is the annihilation operator for a fermion in spin state σ at site $i=(i_{x},i_{y})$ and $w_{i}(x)$ is the corresponding Wannier function [52]. Furthermore, we assume that the detuning Δ_{c} and the cavity damping rate κ are much larger than the recoil frequency $\omega_{r}=\hbar k_{c}^{2}/2m$ of an atom of mass m, making the cavity field dynamics evolve on a much faster timescale than the center of mass motion of the atoms, thus following the latter adiabatically [67]. Consequently, the dynamics of the cavity mode can be simplified by using a steady-state solution and inserting it into (3), which finally leads to the following extended Fermi-Hubbard Hamiltonian

$$\hat{H} = \hat{H}_{HB} - \frac{U_l}{2} \left(\sum_{i,j} (-1)^{|i|} \hat{n}_{i\sigma} \right)^2, \tag{5}$$

$$\hat{H}_{\text{HB}} = -\sum_{ij\sigma} t_{ij} \hat{c}^{\dagger}_{i\sigma} \hat{c}_{j\sigma} + U_s \sum_{i} \hat{n}_{i\uparrow} \hat{n}_{i\downarrow} - \sum_{i\sigma} \tilde{\mu}_{\sigma} \hat{n}_{i\sigma},$$
(6)

where we have defined $\hat{n}_{i\sigma} = \hat{c}^{\dagger}_{i\sigma}\hat{c}_{i\sigma}$. The first term of $\hat{H}_{\rm HB}$ represents the tunneling amplitude, with $t_{ij} = t$ if i,j are nearest neighbors and zero otherwise, while the second term corresponds to the Hubbard onsite interaction of strength U_s . The chemical potential $\tilde{\mu}_{\sigma} = \mu_{\sigma} - \hbar V_0 B$ is displaced with a shift proportional to the overlap of the pump-lattice with the Wannier functions $B = \int \mathrm{d}^3 x \, |w_i(x)|^2 \cos^2(ky)$. The second term in (5) corresponds to the cavity-mediated long-range interactions and is proportional to the square of the occupation imbalance operator

$$\hat{\Theta} \equiv \frac{1}{N_s} \sum_{i\sigma} (-1)^{|i|} \hat{n}_{i\sigma}, \tag{7}$$

where $|i| = i_x + i_y$, multiplied by the density-density interaction strength $U_l = -4\hbar A^2 \Delta_c \eta_0^2/(\Delta_c^2 + \kappa^2)$, where $A = \int \mathrm{d}^3 x \, |w_i(x)|^2 \eta(x)/\eta_0$. Notably, unlike standard extended Hubbard models with nearest-neighbor interactions, the density-density interactions in (5) are of infinite range. By tuning the depth of the static optical lattice $V_{2\mathrm{D}}$ and the pump-cavity detuning Δ_c , the strength of the tunneling t, short- and long-range interactions U_s and U_l can be adjusted [59, 68–72]. We assume a red relative detuning $\Delta_c < 0$, such that $U_l > 0$. As demonstrated in [73], the relaxation rate of the atomic ensemble is suppressed when the ratio ω_r/κ becomes small, which justifies using thermal-equilibrium approaches to describe the steady-state of the atomic system. In the following we describe the RDMFT method used in our analysis.

III. REAL-SPACE DYNAMICAL MEAN-FIELD THEORY

The infinite range of the cavity-mediated long-range interactions in (5) justifies applying a static mean-field decoupling $\hat{\Theta}^2 \approx 2\langle \hat{\Theta} \rangle \hat{\Theta} - \langle \hat{\Theta} \rangle^2$, where the expectation value $\langle \hat{\Theta} \rangle$ has to be determined self-consistently within an iterative algorithm. This expectation value measures the imbalance between the occupations of even (|i| = 2p with $p \in \mathbb{N}_0$) and odd (|i| = 2p + 1 with $p \in \mathbb{N}_0$) lattice sites, thus serving as an order parameter for the emergence of the checkerboard density order. This static mean-field decoupling of the cavity-mediated long-range interaction has been applied to ultracold bosons coupled to a cavity and turned out to be a good approximation to capture the quantum phase transitions present in such systems [53– 56, 59. Within this approximation the density-density long-range interaction reduces to an effective local staggered potential, and the system can be described by the mean-field Hamiltonian

$$\hat{H}_{\rm MF} = \hat{H}_{\rm HB} - N_s U_l \langle \hat{\Theta} \rangle \sum_{i\sigma} (-1)^{|i|} \hat{n}_{i\sigma} + N_s^2 \frac{U_l}{2} \langle \hat{\Theta} \rangle^2. \tag{8}$$

To calculate the equilibrium phase diagram of the system described by $H_{\rm MF}$, we use real-space dynamical mean-field theory (RDMFT), which provides a nonperturbative treatment of strongly correlated lattice systems [65] by fully incorporating the dynamics of local quantum fluctuations at each site which are induced by short-range interactions. The RDMFT framework is an extension of standard dynamical mean-field theory (DMFT) [74] where the strongly correlated N_s site lattice problem is mapped to a set of N_s single-impurity Anderson models, which are coupled by a self-consistency condition [65, 75]. The self consistency in this approach is formulated in real space and relies on assuming a position-dependent local self-energy. A derivation of (real space) DMFT can be obtained by first writing the partition function for the system in the coherent-state pathintegral representation and choosing a single lattice site *i*, which is denoted as the impurity site, and proceeding by integrating out all other degrees of freedom [74]. In the limit of an infinite lattice coordination number z, with the proper rescaling of the hopping amplitude as $t \to t^*/\sqrt{z}$, the effective impurity problem of lattice site *i* can be described by the effective action

$$S_{\text{eff}}^{(i)} = -\int_0^\beta d\tau \int_0^\beta d\tau' \sum_{\sigma} c_{i\sigma}^*(\tau) \mathcal{G}_{\sigma}^{(i)}(\tau - \tau')^{-1} c_{i\sigma}(\tau)$$
$$+ U \int_0^\beta d\tau n_{i\uparrow}(\tau) n_{i\downarrow}(\tau), \tag{9}$$

where $\tau \in [0, \beta]$ is imaginary time, $\beta = 1/T$ is the inverse temperature, and we assume $\hbar = k_{\rm B} = 1$. The fields $c_{i\sigma}(\tau)$ and $c_{i\sigma}^*(\tau)$ are Grassmann variables and we define $n_{i\sigma}(\tau) = c_{i\sigma}^*(\tau)c_{i\sigma}(\tau)$. The Weiss mean-field $\mathcal{G}_{\sigma}^{(i)}(\tau - \tau')$ represents the effect of all other sites on site i. To solve the impurity problem, the effective action (9) is mapped onto an effective Anderson impurity Hamiltonian, chosen to be of the form

$$\hat{H}^{(i)} = -\sum_{\sigma} \gamma_{\sigma}^{(i)} \hat{d}_{\sigma}^{\dagger} \hat{d}_{\sigma} + U_{s} \hat{d}_{\uparrow}^{\dagger} \hat{d}_{\uparrow} \hat{d}_{\downarrow}^{\dagger} \hat{d}_{\downarrow} + \sum_{b\sigma} \epsilon_{b\sigma}^{(i)} \hat{c}_{b\sigma}^{\dagger} \hat{c}_{b\sigma} + \sum_{b\sigma} (v_{b\sigma}^{(i)} \hat{d}_{\sigma}^{\dagger} \hat{c}_{b\sigma} + \text{h.c.}),$$
(10)

where the operators $\hat{d}_{\sigma}^{(\dagger)}$ act on the impurity site and the operators $\hat{c}_{b\sigma}^{(\dagger)}$ act on the bath orbitals labeled by the index b. The impurity orbital energy is defined as $-\gamma_{\sigma}^{(i)} = -\tilde{\mu}_{\sigma} - (-1)^{|i|} N_s U_l \langle \hat{\Theta} \rangle$. For a given Weiss mean-field $\mathcal{G}_{\sigma}^{(i)}$ and a given initial occupation imbalance (set to $\langle \hat{\Theta} \rangle \approx 0.2$ in all our calculations), the algorithm proceeds by fitting the energies of the bath orbitals $\epsilon_{b\sigma}^{(i)}$ and the couplings between bath and impurity orbitals $v_{b\sigma}^{(i)}$ to reproduce the first term of the effective local action (9) via

$$\mathcal{G}_{\sigma}^{(i)}(\mathrm{i}\omega_m)^{-1} = \mathrm{i}\omega_m + \gamma_{\sigma}^{(i)} + \sum_{h} \frac{|v_{b\sigma}^{(i)}|^2}{\epsilon_{h\sigma}^{(i)} - \mathrm{i}\omega_m}, \tag{11}$$

where $\omega_m=(2m+1)\pi/\beta$ are fermionic Matsubara frequencies with $m\in\mathbb{Z}$. Using the resulting values of $\epsilon_{b\sigma}^{(i)}$ and $v_{b\sigma}^{(i)}$, we construct the effective impurity Hamiltonian (10) and solve it by exact diagonalization, where we have to assume that the number of bath orbitals is finite to limit the Hilbert-space dimension. This method has the advantage of giving access to the real frequency spectrum without the need for numerical analytic continuation. By calculating the eigenstates $|n^{(i)}\rangle$ and eigenenergies $E_n^{(i)}$ of (10), we obtain the impurity Green's function in the Lehmann representation

$$G_{\sigma}^{(i)}(i\omega_m) = \frac{1}{\mathcal{Z}^{(i)}} \sum_{l,n} \frac{(e^{-\beta E_l^{(i)}} + e^{-\beta E_n^{(i)}}) |\langle l^{(i)} | d_{\sigma}^{\dagger} | n^{(i)} \rangle|^2}{i\omega_m + E_l^{(i)} - E_n^{(i)}},$$
(12)

and use the local Dyson equation to compute the position dependent local self-energy in real space

$$\Sigma_{i,\sigma}(i\omega_m) = \mathcal{G}_{\sigma}^{(i)}(i\omega_m)^{-1} - G_{\sigma}^{(i)}(i\omega_m)^{-1}. \tag{13}$$

Here, $\mathcal{Z}^{(i)} = \sum_n e^{-\beta E_n^{(i)}}$ is the partition function of the impurity model. The interacting lattice Green's function is then calculated from the lattice Dyson equation

$$[\mathbf{G}_{\sigma}(\mathrm{i}\omega_m)]^{-1} = (\tilde{\mu}_{\sigma} + \mathrm{i}\omega_m)\mathbf{1} + \mathbf{t} + \mathbf{V} - \mathbf{\Sigma}_{\sigma}(\mathrm{i}\omega_m), \quad (14)$$

where we use bold symbols to represent real space matrices labeled by lattice site indices i, j. Here, 1 is the identity matrix, t is the hopping matrix with elements t_{ij} , and **V** with matrix elements $V_{ij} = \delta_{ij}V_i =$ $\delta_{ii}(-1)^{|i|}N_sU_l\langle\hat{\Theta}\rangle$ represents a spatially varying potential, which arises due to the mean-field decoupling of the cavity-mediated long-range interactions. The local self-energy is diagonal in real space with matrix elements $[\Sigma_{\sigma}(i\omega_m)]_{ij} = \delta_{ij}\Sigma_{i,\sigma}(i\omega_m)$. Self consistency is achieved by equating the diagonal elements of the lattice Green's function with the local impurity Green's function, i.e. $G_{\sigma}^{(i)}(i\omega_m) = [\mathbf{G}_{\sigma}(i\omega_m)]_{ii}$, and subsequently calculating the Weiss mean field from the local Dyson equation (13). Solving the impurity problem allows us to calculate the local on-site occupations, which we use to obtain the occupation imbalance $\langle \Theta \rangle$ updated in the simulation after each RDMFT iteration. Methods based on DMFT are exact only in the limit of infinite dimensions (or equivalently, large coordination number). However, they provide a reliable approximation for studying the phases of finite-dimensional lattice systems such as the one considered here, as has been consistently demonstrated in numerous applications (see, for instance, Refs. [15, 20, 25, 27, 28, 34]).

RDMFT allows us to describe inhomogeneous correlated lattice systems, but it requires more computational resources than standard DMFT. This is because the lattice Dyson equation (14) involves the inversion of $N_s \times N_s$ matrices and because for every lattice site an effective quantum impurity problem needs to be solved. The latter task can be significantly simplified using insight from the

expected type of symmetry breaking. The transition to the checkerboard density-wave phase corresponds to a \mathbb{Z}_2 parity-symmetry breaking [36] towards a bipartite structure with finite occupation imbalance $\langle \hat{\Theta} \rangle$ between even and odd lattice sites. After confirming this translational-symmetry breaking with unbiased RDMFT for a system of size $N_s = 8 \times 8$, we have applied a unit-cell procedure [76] which assumes that all sites within the same sublattice (even or odd) are equivalent. This reduces the number of different quantum impurity problems to one per sublattice, while the lattice Green's function is still computed for the full system via (14). This allowed us to simulate lattices of size $N_s = 32 \times 32$ with reduced computational cost, thus minimizing finite-size effects.

IV. RESULTS AND DISCUSSION

As previously discussed, the occupation imbalance $\langle \hat{\Theta} \rangle$ serves as an order parameter for the checkerboard density-wave phase marking the self-organization of the atoms on the even or odd lattice sites. On the other hand, the paramagnetic Mott transition can be characterized by the quasiparticle residue which measures the spectral weight at the Fermi level and becomes zero at the critical point marking the absence of quasiparticles in the Mott insulator phase and the vanishing of the metallic DMFT solution [74]. For each sublattice, we obtain the quasiparticle residue from the converged self-energy via [30, 77]

$$Z_{\mathbf{e},\mathbf{o}} = \left(1 - \frac{\mathrm{Im}\Sigma_{\mathbf{e},\mathbf{o}}(\mathrm{i}\omega_0)}{\omega_0}\right)^{-1},\tag{15}$$

where the indices **e** and **o** correspond to sites in the even and odd sublattices, respectively, and we have suppressed the spin index assuming $\Sigma_{i,\uparrow}(\mathrm{i}\omega_m) = \Sigma_{i,\downarrow}(\mathrm{i}\omega_m) = \Sigma_i(\mathrm{i}\omega_m)$, which is valid for the paramagnetic phases studied here. Overall, we characterize the emerging phases of the systems as follows:

- i) The homogeneous Fermi-liquid phase (FL) is characterized by a finite value of $Z_{\mathbf{e},\mathbf{o}}$ corresponding to a quasiparticle peak at the Fermi level, while the occupation imbalance vanishes, i.e. $\langle \hat{\Theta} \rangle = 0$.
- ii) In the paramagnetic Mott insulating phase (MI) the absence of quasiparticles is marked by $Z_{\mathbf{e},\mathbf{o}} = 0$ and each site has the same average density, i.e. $\langle \hat{\Theta} \rangle = 0$.
- iii) In the density-wave phase (DW) the imbalance $\langle \hat{\Theta} \rangle$ is finite. At quarter filling and for low temperatures the DW phase remains metallic [15] while at half filling its single-particle spectrum is always gapped due to the checkerboard potential [34], similarly to a band insulator. The quasiparticle residue is finite in this phase, i.e. $Z_{\mathbf{e},\mathbf{o}} > 0$.

For all calculations, we have introduced an initial value of the staggered potential corresponding to $\langle \hat{\Theta} \rangle \approx 0.2$ for starting the RDMFT iterations. Furthermore, we use a lattice of size $N_s = 32 \times 32$ and set t = 1, i.e. the hopping amplitude is the unit of energy.

Extended Hubbard models at quarter filling are particularly relevant because they represent the simplest model that reproduces the interplay between charge order and superconductivity in layered molecular crystals such as bis-(ethylenedithia-tetrathiafulvalene) (BEDT-TTF) [24, 78, 79]. For nearest-neighbor repulsion and considering a Bethe lattice with infinite connectivity it was demonstrated in [15], using infinite-system-size DMFT, that this model exhibits reentrant behavior in the transition from a homogeneous metallic to a chargeordered phase for increasing temperature at quarter filling. More recently, the extended Hubbard model with nearest-neighbor interactions on a Bethe lattice was investigated for general filling at zero temperature in [34] using infinite-system-size DMFT. The authors mapped the phase diagram as a function of chemical potential. short- and nearest-neighbor interaction, identifying the existence of a Fermi liquid, a Mott insulator, half- and quarter-filled charge-ordered insulators, and a chargeordered metal. In particular, upon varying short- and long-range interaction strength at half filling, they obtained a phase diagram featuring regions of metastability in which half-filled charge-ordered solution obtained in DMFT coexists with either the homogeneous Fermi-liquid or the Mott-insulating solution. Motivated by the possibility of realizing similar physics in a different setting across the superrandiant self-organization phase transition analyzed here, we investigated both quarter filling $(\sum_{i} \langle \hat{n}_{i\uparrow} \rangle = \sum_{i} \langle \hat{n}_{i\downarrow} \rangle = N_s/4)$ and half filling $(\sum_{i} \langle \hat{n}_{i\uparrow} \rangle = \sum_{i} \langle \hat{n}_{i\downarrow} \rangle = N_s/2)$ cases and investigated the effect of varying temperature and long-range interactions for fixed short-range interaction strengths. Furthermore, for a fixed low temperature and half filling we studied the phase transitions for different U_s and U_l and determined the phase diagram.

In Fig. 2a) the quarter filling T- U_l -phase diagram for $U_s = 16$ is shown. We found a transition from a homogeneous FL phase into a DW phase. The curve for the critical long-range interaction strength as a function of temperature $U_I^c(T)$ shows a negative slope for T < 0.4. This implies that in the interval $3.96 < N_s U_l < 5.07$, increasing temperature leads to a crystallization of the FL phase into a DW phase. As we have neglected the possibility of magnetic ordering, at quarter filling the entropy of the spin degrees of freedom for each occupied site in the deep DW phase is approximately ln 2. Hence, the entropy contribution reduces the free energy in the DW by a larger amount in contrast to the entropy of the FL state which is proportional to T [15, 74], thus leading to the FL-DW transition with increasing temperature. Further increasing T leads to the expected melting of the DW phase and a reentrance into the homogeneous FL phase.

In Fig. 2b) and c) we show the corresponding phase

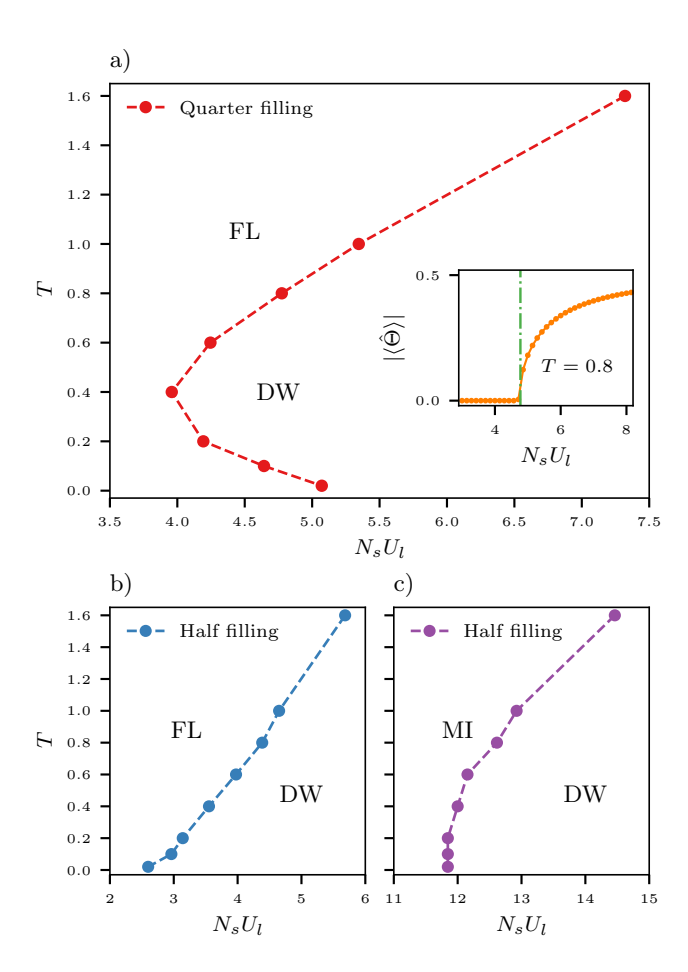


FIG. 2. Phase diagram of the extended Fermi-Hubbard model with cavity-mediated long-range interactions at quarter and half filling in the T- U_l -plane. The distinct phases are denoted as: FL (homogeneous Fermi liquid), MI (Mott insulator), DW (checkerboard density-wave). For both a) and the c) the short-range interaction strength is fixed at $U_s = 16$, while for b) its value is $U_s = 3$. At quarter filling a) we observe reentrant behavior at low temperatures. In contrast, no such behavior is present at half filling, i.e. in b) and c). The inset in a) shows the U_l dependence of the occupation imbalance $\langle \hat{\Theta} \rangle$ at temperature T = 0.8 where the green dot-dashed line marks the FL-DW transition at $N_s U_l = 4.77$.

diagram at half filling. The FL-DW transition can be observed in Fig. 2b) for $U_s=3$, while the transition from the Mott insulator state (MI) to the DW state is shown in Fig. 2c) for $U_s=16$. At half filling, when the occupation imbalance asymptotically approaches its maximum value, i.e. $\langle \hat{\Theta} \rangle \approx \pm 1$, the DW phase consists of one approximately empty sublattice and the other approximately doubly occupied, forming local singlets with no spin degeneracy and, hence, zero entropy. Thus, at low temperatures and half filling, the transition from FL to DW with increasing temperature is disfavored, since the FL entropy is proportional to T, lowering the free energy relative to the one deep in the DW phase where the entropy is approximately zero. For strong short-range in-

teraction, deep in the paramagnetic MI phase, each site is singly occupied with a spin degeneracy of two, resulting in an entropy of $\ln 2$ per site. Thus, similarly to previous case, the transition from MI to DW with increasing temperature is suppressed, as the finite entropy of the MI phase leads to a lower free energy than the deep DW phase where the entropy is zero. As a result, there is no entropic advantage to forming DW order upon heating, so $U_l^c(T)$ has a positive slope and no reentrant behavior occurs at half filling. We point out that with increasing temperature the FL and MI phases are expected to undergo a crossover into a bad metal and a bad insulator state, respectively [80]. However, the occupation imbalance $\langle \hat{\Theta} \rangle$ still serves as an order parameter for the transition into the DW state.

For half filling and fixed temperature (T = 0.02) we have investigated the phase transitions as a function of U_l and U_s . In the absence of Hubbard short-range interactions $(U_s = 0)$, the DW phase already emerges for vanishingly small long-range interaction strength (Fig. 3a)). This is due to the perfect nesting of the Fermi surface at half filling on a square lattice [49– 51]. As demonstrated in [51] for non-interacting spinless fermions, the critical pump-cavity coupling strength for the superradiant self-organization phase transition is inversely proportional to the fermionic density-density susceptibility. For $U_s = U_l = 0$, i.e. noninteracting spinful fermions on a half-filled square lattice, the densitydensity susceptibility shows a strong response for zeroenergy excitations at the wave vector $\mathbf{q} = (\pi, \pi)$. This response decreases for increasing U_s [31] while keeping $U_l = 0$. In the commensurate configuration between cavity, pump and static square optical lattice ($k_p \approx k_c =$ $k_{\text{latt}} = k$), the cavity-mediated long-range interactions couple to the atomic density exactly at q. In particular, the sum in the second term of (5) can be written as

$$\sum_{i\sigma} (-1)^{|i|} \hat{n}_{i\sigma} = \sum_{i\sigma} e^{iq \cdot i} \hat{n}_{i\sigma}.$$
 (16)

The strong density-density response of noninteracting fermions on a square lattice at half filling for zero energy excitations at the nesting vector \mathbf{q} leads to the onset of the density wave phase at arbitrarily small U_l .

The full phase diagram at half filling is shown in Fig. 4a). For small short-range interactions, increasing U_l leads to a FL-DW transition. In this region of small U_s and U_l , the FL-DW phase boundary remains close to the line $N_sU_l=U_s$. For small U_l , increasing the Hubbard short-range interactions U_s from intermediate to strong, leads to a FL-MI transition, where the critical value U_s^c remains constant for increasing U_l (see red square markers). This is because in this regime the mean-field Hamiltonian (8) reduces to the standard Fermi-Hubbard model due the vanishing imbalance, i.e. $\langle \hat{\Theta} \rangle = 0$. The critical Hubbard interaction for the FL-MI transition, obtained from the vanishing of $Z_{\mathbf{e},\mathbf{o}}$ depicted in Fig. 3b), remains at $U_s^c = 10.3$ independent of U_l (red square markers). We point out that at low temperatures, DMFT cal-

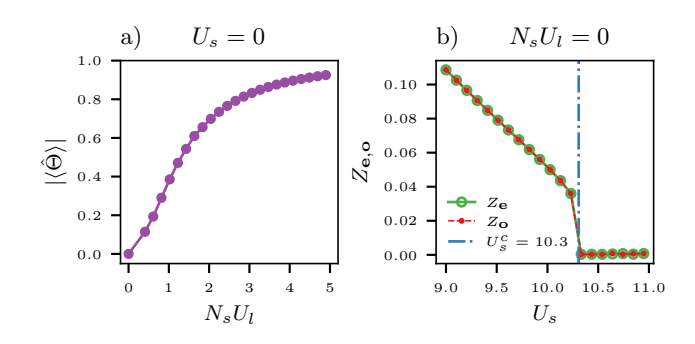


FIG. 3. a) Occupation imbalance $\langle \hat{\Theta} \rangle$ for increasing longrange interaction strength U_l at half filling, for $U_s=0$ and T=0.02. Due to the perfect nesting of Fermi surface, the imbalance becomes finite as soon as the long-range interactions are non zero signaling the transition to the density-wave phase. b) Quasiparticle weight $Z_{\mathbf{e},\mathbf{o}}$ as a function of the shortrange interaction strength U_s at half filling, for $U_l=0$ and T=0.02. The paramagnetic Mott transition is characterized by a linear decrease of $Z_{\mathbf{e},\mathbf{o}}$ for increasing U_s until it becomes zero at $U_s^c=10.3$ (dot-dashed green line) marking the vanishing of the Fermi liquid solution obtained using RDFMT.

culations predict a region across the paramagnetic Mott transition where both the FL and the MI solution coexist [74, 80]. At zero temperature and for $U_l = 0$, the thermodynamic FL-MI phase transition occurs precisely at the critical Hubbard interaction U_s^c which is determined by the breakdown of the FL solution obtained using DMFT. We therefore use this criterion to determine the FL-MI transition within RDMFT.

For sufficiently large U_s , increasing the long-range interaction U_l drives a MI-DW transition. We found a region in the phase diagram highlighted as light pink (yellow) shaded areas in Fig. 4 where the MI (FL) solution coexists with the DW solution. The expected thermodynamic phase transition can be understood by analyzing the model in atomic limit of t = 0 at zero temperature [56, 60]. In this limit, the eigenstates of the Hamiltonian (5) are Fock states with well-defined number of particles at each site. Assuming half filling and a given finite occupation imbalance $\langle \Theta \rangle > 0$, the competition between U_s and U_l leads to the formation of domains, where a fraction $|\langle \Theta \rangle|$ of the sites is in the DW domain while the remaining fraction is in the MI domain. The energy per particle (per site) of such a state has the following form (see appendix A)

$$\frac{\langle \hat{H} \rangle}{N_s} = \frac{U_s}{2} |\langle \hat{\Theta} \rangle| - \frac{N_s U_l}{2} \langle \hat{\Theta} \rangle^2 - \tilde{\mu}, \tag{17}$$

In the $T \to 0$ limit, the grand potential of the system is given by $\langle \hat{H} \rangle$. If the ratio between long- and short-range interaction strengths is small, i.e. $N_s U_l/U_s \ll 1$, Eq. (17) has a single minimum corresponding to a MI state with zero imbalance ($\langle \hat{\Theta} \rangle = 0$). When the long-range interactions are increased such that $N_s U_l/U_s > 1$, the expectation value $\langle \hat{H} \rangle$ in (17) acquires two minima

at $\langle \hat{\Theta} \rangle = \pm 1$ which correspond to a DW state. However, if $N_s U_l / U_s \approx 1$, the minima of (17) at $\langle \hat{\Theta} \rangle = 0$ and at $\langle \hat{\Theta} \rangle = \pm 1$ become close in energy (see appendix A). A similar atomic-limit argument was used in [56] where lattice bosons coupled to a transversely pumped cavity were studied with bosonic DMFT, and where an analogous coexistence region was found. Subsequently, the metastability of these two states was observed experimentally in [60] in the bosonic case.

In the vicinity of the line $N_s U_l/U_s \approx 1$, for strong (intermediate) U_s values, we find that initializing the RDMFT iterations from the MI (FL) phase and increasing U_l leads to a larger critical value U_l^c for the MI-DW (FL-DW) transition (orange empty circle markers in Fig. 4a)) than starting from the DW phase and decreasing U_l for a fixed U_s (purple circle markers in Fig. 4a)), which means that there is a coexistence region for the homogeneous MI (FL) and DW solutions obtained within RDMFT. For moderate values of U_s and U_l , we find an FL-DW coexistence region (yellow shaded area) while for strong U_s and U_l we find a MI-DW coexistence region (light-pink shaded area). A similar result was found in [34] for the extended Hubbard model with nearest neighbor interactions on Bethe lattice. The hysteretic behavior of the imbalance $\langle \hat{\Theta} \rangle$ for the different RDMFT solutions at $U_s = 12$ is presented in Fig. 4b).

To calculate the thermodynamic transition, we follow the approach used in [56], approximating the grand potential by the expectation value of the effective meanfield Hamiltonian (8), i.e. $\Omega \approx \langle \hat{H}_{\rm MF} \rangle$, and neglecting the contribution -TS, where S is the entropy. This approximation becomes exact only in the limit of zero temperature, however for the temperature T = 0.02 chosen in the phase diagram shown in Fig. 4, the maximum value of the term -TS contributing to the grand potential is less than 0.3% of the energy. Hence, this approximation has negligible influence on the prediction of the thermodynamic phase transition. In RDMFT, the expectation values of the local terms in the Hamiltonian (8) are obtained directly from the exact diagonalization of the effective impurity Hamiltonian (10). In appendix B, we demonstrate how the kinetic energy corresponding to the expectation value of the tunneling term in (8) can be calculated from local quantities in RDMFT. In Fig. 4c), where $U_s = 12$, one observes that the energy of the DW solution decreases linearly with U_l within the coexistence region and becomes lower than the energy of the MI solution at $U_l = 11.6$ where the thermodynamic MI-DW phase transition takes place. The blue diamond-shaped markers in Fig. 4a) show the thermodynamic phase transition, which agrees well with the line $N_sU_l=U_s$ (dotted black line) obtained from the atomic limit analysis of the model. For the system sizes investigated (8×8 , 16×16 , 32×32), no significant finite-size effects were observed for this phase boundary as well as for the boundaries of the coexistence region.

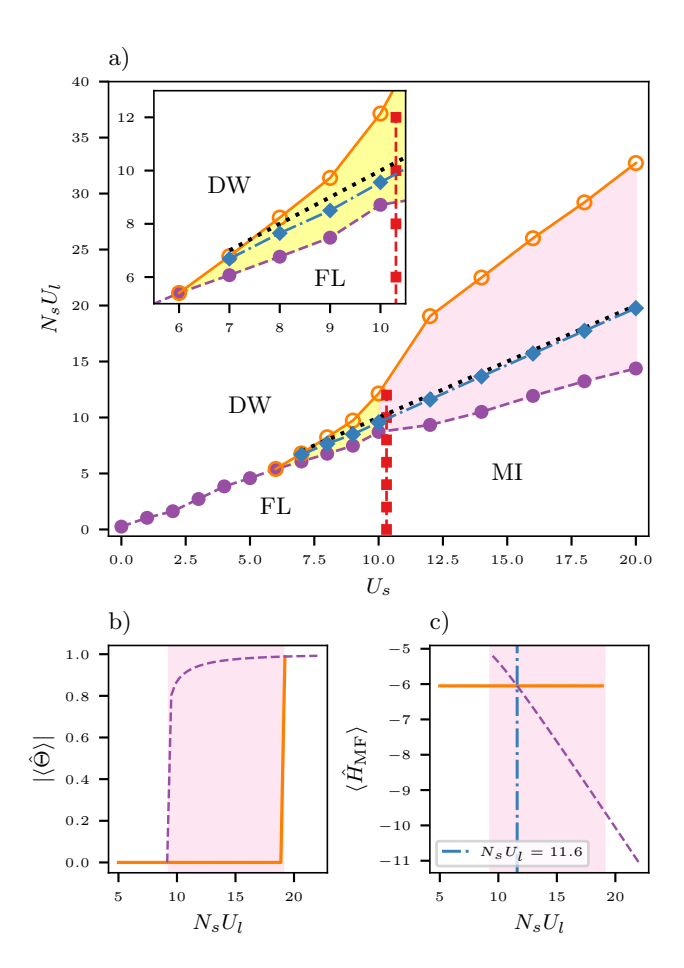


FIG. 4. a) Phase diagram of the extended Fermi-Hubbard model with cavity-mediated long-range interactions at half filling and for T = 0.02. The distinct phases are denoted as: FL (homogeneous Fermi liquid), MI (Mott insulator), DW (checkerboard density-wave). The FL-MI transition is marked by red squares. The purple circle dots correspond to the border of the region of metastability of the DW solution obtained within RDMFT, while the orange empty circles represent the border of the region of metastability of the homogeneous FL and MI solutions. The region where the MI and DW solutions coexist is depicted in shaded pink, while the region where the FL and DW solutions coexist is represented by the yellow shaded area. The inset shows a zoom into the FL-DW coexistence region. The diamond blue markers represent the thermodynamic phase transition obtained by comparing the energies of the homogeneous FL and MI solutions with the DW solution obtained within RDMFT. These points follow closely the dotted black line $N_sU_l = U_s$ obtained by analyzing the model in the atomic limit. Plots b) and c) show the hysteretic behavior of the occupation imbalance $|\langle \Theta \rangle|$ and the expectation value of the mean-field Hamiltonian $\langle \hat{H}_{\rm MF} \rangle$ (Eq. (8)) for $U_s = 12$ and T = 0.02, respectively. In b) and c) the dashed purple line indicates the DW solution while the continuous orange line corresponds to the MI solution. The thermodynamic phase transition is indicated in c) by the vertical dot-dashed blue line at $N_sU_l = 11.6$.

V. CONCLUSION

We have investigated the phases of the extended Fermi-Hubbard model with cavity-mediated long-range interactions on a square lattice, both at half and quarter filling, using RDMFT. We included the long-range interactions via a static mean-field decoupling. At quarter filling, we found a phase transition between a homogeneous Fermiliquid phase and a checkerboard density-wave phase as the long-range interaction strength is increased. Additionally, we observed reentrant behavior in a region of the phase diagram where the systems undergoes a phase transition from the homogeneous Fermi-liquid phase to the density-wave phase and back to the homogeneous Fermi-liquid phase as temperature is increased. This result is similar to previous DMFT results for the extended Hubbard model with nearest-neighbors interaction [15]. At half filling, we found that for small Hubbard- and long-range interactions a Fermi-liquid phase exists. However, for vanishing Hubbard U_s the instability of this phase towards a checkerboard density-wave insulating phase occurs for arbitrarily small long-range interaction strengths. This is due to the perfect nesting of the Fermi surface at half filling [49–51]. For intermediate and strong Hubbard U_s and long-range interactions U_l , we observe a coexistence region in the phase diagram where the homogeneous Fermi-liquid, Mott insulating, and density wave solutions of RDMFT are metastable. We observed that the occupation imbalance shows hysteretic behavior in the coexistence region, which is characteristic of a firstorder phase transition. By comparing the energy of the different RDMFT solutions in that region, we determined the thermodynamic phase boundary for the transition into the density-wave phase.

ACKNOWLEDGMENTS

This work was funded by the Deutsche Forschungsgemeinschaft (DFG, German Research Foundation) under Project No. 557989325, as an individual grant (Sachbeihilfe) with the project ID HO 2407/12-1. The authors gratefully acknowledge the computing time provided to them at the NHR Center NHR@SW at Goethe University Frankfurt. This is funded by the Federal Ministry of Education and Research, and the state governments participating on the basis of the resolutions of the GWK for national high performance computing at universities (www.nhr-verein.de/unsere-partner). The authors gratefully acknowledge the Gauss Centre for Supercomputing e.V. (www.gauss-centre.eu) for funding this project by providing computing time through the John von Neumann Institute for Computing (NIC) on the GCS Supercomputer JUWELS at Jülich Supercomputing Centre (JSC).

Appendix A: Metastability in the atomic limit

In this section we present a derivation justifying the metastability found in our results by analyzing the expectation value for the effective Hamiltonian (5) in the atomic limit, following [56, 60]. In this limit, we have t=0, and the effective Hamiltonian (5) assumes the following form

$$\hat{H} = U_s \sum_{i} \hat{n}_{i\uparrow} \hat{n}_{i\downarrow} - \frac{U_l}{2} \left(\sum_{i\sigma} (-1)^{|i|} \hat{n}_{i\sigma} \right)^2 - \sum_{i\sigma} \tilde{\mu}_{\sigma} \hat{n}_{i\sigma}.$$
(A1)

At half filling for a balanced configuration between the spins, we have that $\tilde{\mu}_{\uparrow} = \tilde{\mu}_{\downarrow} \equiv \tilde{\mu}$ and $\sum_{i} \langle \hat{n}_{i\uparrow} \rangle =$ $\sum_{i} \langle \hat{n}_{i\downarrow} \rangle = N_s/2$. In this case, due to the interplay between U_s and U_l the system forms DW and MI domains, with a fraction $f_{\rm DW} = |\langle \hat{\Theta} \rangle|$ of the sites being in the DW domain while the remaining fraction is in the MI domain. For the square lattice geometry, both the number of even sites and the number of odd sites are equal to $N_s/2$. Assuming that the DW domain self-organizes on the even sites, the number of particles on the even sites is $N_e = N_s/2 + N_d$ while the number of particles on the odd sites is $N_o = N_s/2 - N_d$, where N_d is the number of doubly occupied sites. The average occupation imbalance is then $\langle \hat{\Theta} \rangle = (N_e - N_o)/N_s = 2N_d/N_s$. Since the DW fraction may also self-organize on the odd sites, we have that the number of doubly occupied sites becomes $N_d = |\langle \Theta \rangle| N_s/2 = f_{\rm DW} N_s/2$. The doubly occupied sites increase the system's energy due to the onsite Hubbard interaction U_s , so that the expectation value of the shortrange interaction term becomes

$$U_s \sum_{i} \langle \hat{n}_{i\uparrow} \hat{n}_{i\downarrow} \rangle = U_s N_d = \frac{1}{2} U_s f_{\text{DW}} N_s.$$
 (A2)

Thus, the expectation value of the Hamiltonian (A1) can be written as,

$$\frac{\langle \hat{H} \rangle}{N_s} = \frac{U_s}{2} |\langle \hat{\Theta} \rangle| - \frac{N_s U_l}{2} \langle \hat{\Theta} \rangle^2 - \tilde{\mu}, \tag{A3}$$

where we have assumed a vanishing variance of the occupation imbalance such that $\langle \hat{\Theta}^2 \rangle = \langle \hat{\Theta} \rangle^2$. In Fig. 5 we plot (A3) for different values of the ratio $N_s U_l/U_s$. As can be observed, for $N_s U_l/U_s < 1$, the atomic limit energy has a minimum at $\langle \hat{\Theta} \rangle = 0$ corresponding to the MI phase. At $N_s U_l/U_s = 1$, the expectation value (A3) shows three minima, one at $\langle \hat{\Theta} \rangle = 0$ and the other two at $\langle \hat{\Theta} \rangle = \pm 1$. For $N_s U_l/U_s > 1$, the minima at $\langle \hat{\Theta} \rangle = \pm 1$ become lower in energy than the local minimum at $\langle \hat{\Theta} \rangle = 0$ leading to the stabilization of a DW phase.

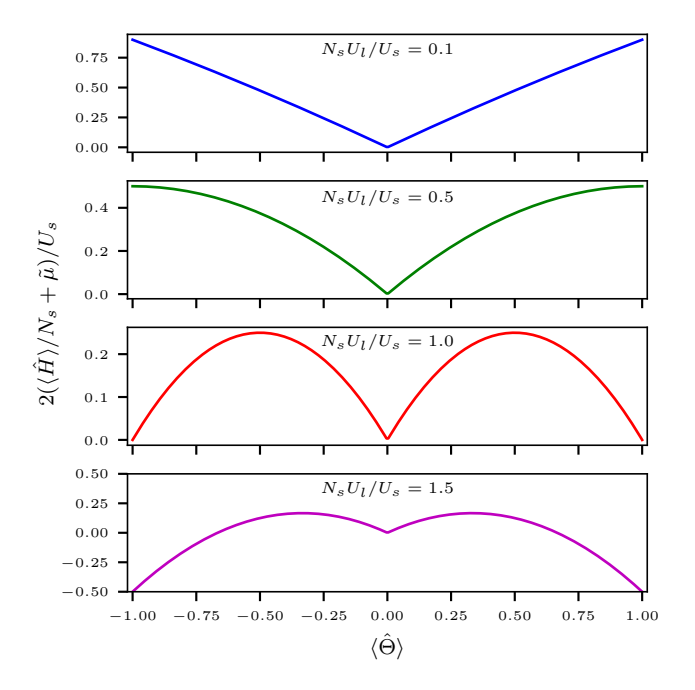


FIG. 5. Expectation value of the energy in the atomic limit Eq. (A1) for different values of the ratio $N_s U_l/U_s$.

Appendix B: Kinetic Energy in RDMFT

Apart from the kinetic energy term contribution to the expectation value of the mean-field Hamiltonian

$$\langle \hat{H}_{\mathrm{MF}} \rangle = -\sum_{ij\sigma} t_{ij} \langle \hat{c}_{i\sigma}^{\dagger} \hat{c}_{j\sigma} \rangle + U_{s} \sum_{i} \langle \hat{n}_{i\uparrow} \hat{n}_{i\downarrow} \rangle - \sum_{i\sigma} \tilde{\mu}_{\sigma} \langle \hat{n}_{i\sigma} \rangle - N_{s}^{2} U_{l} \langle \hat{\Theta} \rangle^{2}$$
(B1)

all other terms are local and can be computed directly from the impurity solver within RDMFT. Following [81], here we show how the expectation value of the kinetic energy can be expressed in terms of local quantities and calculated using RDMFT.

We first point out that, in terms of the imaginary time lattice Green's function, the expectation value of the operators in the hopping term of the mean field Hamiltonian Eq. (8) can be written as

$$\langle \hat{c}_{i\sigma}^{\dagger} \hat{c}_{j\sigma} \rangle = \lim_{\eta \to 0^{+}} [\mathbf{G}_{\sigma}(\tau = -\eta)]_{ji}$$

$$= \frac{1}{\beta} \lim_{\eta \to 0^{+}} \sum_{m} [\mathbf{G}_{\sigma}(i\omega_{m})]_{ji} e^{i\omega_{m}\eta}.$$
(B2)

Thus, the kinetic energy becomes

$$E_{\text{kin}} = -\sum_{ij\sigma} t_{ij} \langle \hat{c}_{i\sigma}^{\dagger} \hat{c}_{j\sigma} \rangle$$

$$= -\frac{1}{\beta} \lim_{\eta \to 0^{+}} \sum_{m} \sum_{ij\sigma} t_{ij} [\mathbf{G}_{\sigma}(i\omega_{m})]_{ji} e^{i\omega_{m}\eta}.$$
(B3)

Making use of the lattice Dyson equation $[\mathbf{G}_{\sigma}(\mathrm{i}\omega_m)]_{ij}^{-1} = [\tilde{\mu}_{\sigma} + \mathrm{i}\omega_m + V_i - \Sigma_{i,\sigma}(\mathrm{i}\omega_m)]\delta_{ij} + t_{ij}$, we note that

$$\sum_{j} [\mathbf{G}_{\sigma}(i\omega_{m})]_{ij}^{-1} [\mathbf{G}_{\sigma}(i\omega_{m})]_{ji} = 1$$

$$\sum_{j} \{ [\tilde{\mu}_{\sigma} + i\omega_{m} + V_{i} - \Sigma_{i,\sigma}(i\omega_{m})] \delta_{ij} + t_{ij} \}$$

$$\times [\mathbf{G}_{\sigma}(i\omega_{m})]_{ji} = 1.$$
(B4)

From the equation above, using the local Dyson equation $\Sigma_{i,\sigma}(i\omega_m) = \mathcal{G}_{\sigma}^{(i)}(i\omega_m)^{-1} - G_{\sigma}^{(i)}(i\omega_m)^{-1}$ and the relation $G_{\sigma}^{(i)}(i\omega_m) = [\mathbf{G}_{\sigma}(i\omega_m)]_{ii}$, it can be demonstrated that

$$-\sum_{j} t_{ij} [\mathbf{G}_{\sigma}(\mathrm{i}\omega_{m})]_{ji} = [\tilde{\mu}_{\sigma} + \mathrm{i}\omega_{m} + V_{i} - \mathcal{G}_{\sigma}^{(i)}(\mathrm{i}\omega_{m})^{-1}] \times G_{\sigma}^{(i)}(\mathrm{i}\omega_{m}).$$
(B5)

Notice that the +1 term on the right-hand side of Eq. (B4) cancels with the one coming from the multiplication of the local Green's function by its inverse $G_{\sigma}^{(i)}(\mathrm{i}\omega_m)^{-1}G_{\sigma}^{(i)}(\mathrm{i}\omega_m)=1$ on the left-hand side which appears after making the substitution of the self-energy using the local Dyson equation. Hence, the kinetic energy can be finally written as

$$E_{\text{kin}} = \frac{2}{\beta} \lim_{\eta \to 0^{+}} \sum_{m \ge 0} e^{i\omega_{m}\eta} \times \sum_{i\sigma} [\tilde{\mu}_{\sigma} + i\omega_{m} + V_{i} - \mathcal{G}_{\sigma}^{(i)}(i\omega_{m})^{-1}] G_{\sigma}^{(i)}(i\omega_{m}).$$
(B6)

Numerically, only a finite number of positive Matsubara frequencies is considered in the calculation which implies that the equal time limit is not obtained by simply imposing $\eta=0$. The solution is found by finding for every site the value of η satisfying the relation

$$\frac{2}{\beta} \lim_{\eta \to 0^{+}} \sum_{m \ge 0} e^{i\omega_{m}\eta} G_{\sigma}^{(i)}(i\omega_{m}) = \langle \hat{n}_{i\sigma} \rangle_{AIM}, \qquad (B7)$$

where $\langle \hat{n}_{i\sigma} \rangle_{\text{AIM}}$ is obtained by solving the Anderson impurity Hamiltonian (10).

In Fig. 6, we show the energy calculated across the MI-DW phase transition for the different MI and DW solutions obtained within RDMFT.

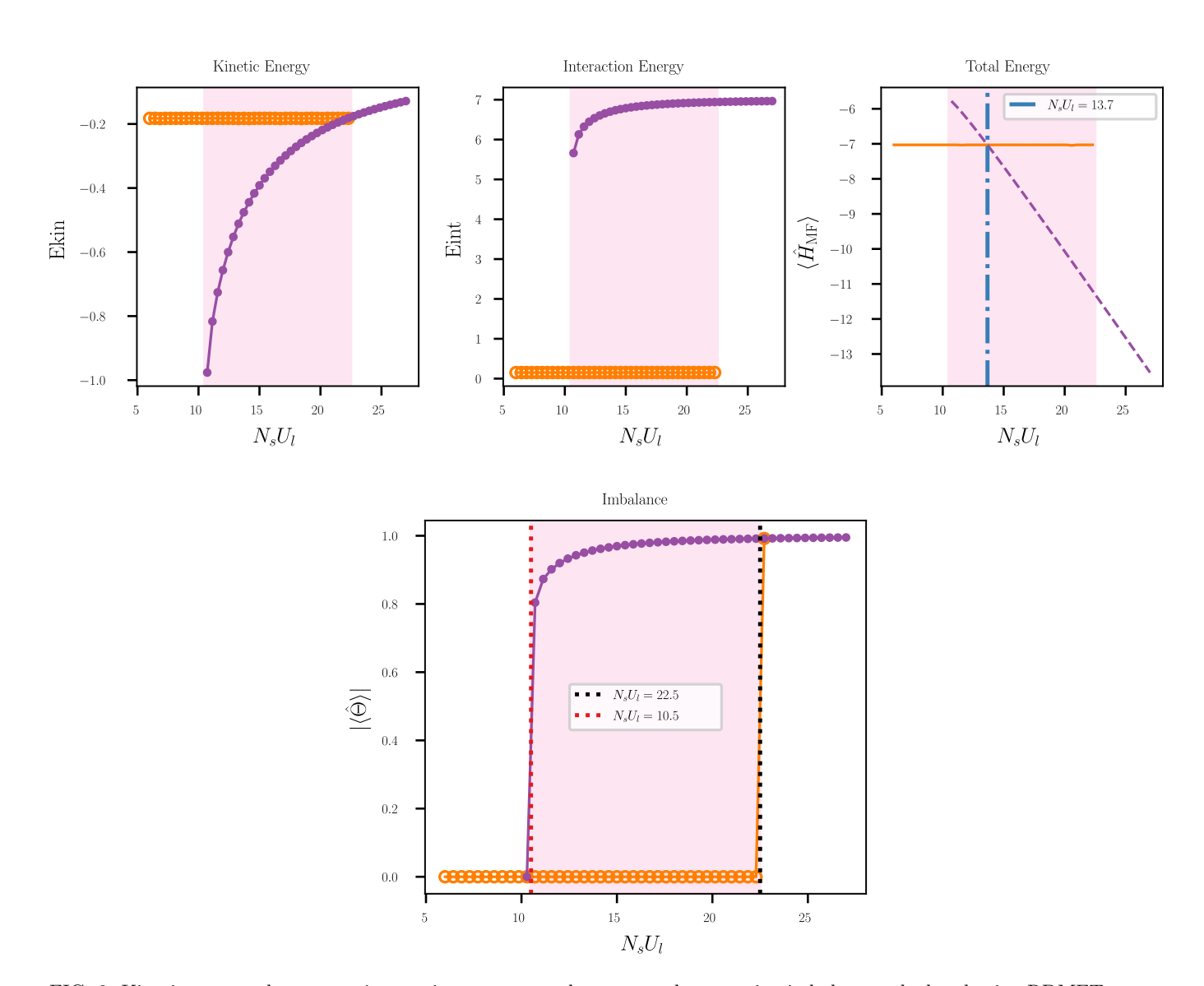


FIG. 6. Kinetic energy, short-range interaction energy, total energy, and occupation imbalance calculated using RDMFT across the MI-DW phase transition for $U_s = 14$ and T = 0.02. The DW solution is shown in purple while the MI solution is shown in orange.

- A. Griesmaier, J. Werner, S. Hensler, J. Stuhler, and T. Pfau, Bose-einstein condensation of chromium, Physical Review Letters 94, 160401 (2005).
- [2] R. Chicireanu, A. Pouderous, R. Barbé, B. Laburthe-Tolra, E. Maréchal, L. Vernac, J.-C. Keller, and O. Gorceix, Simultaneous magneto-optical trapping of bosonic and fermionic chromium atoms, Physical Review A 73, 053406 (2006).
- [3] T. Lahaye, C. Menotti, L. Santos, M. Lewenstein, and T. Pfau, The physics of dipolar bosonic quantum gases, Reports on Progress in Physics 72, 126401 (2009).
- [4] M. A. Baranov, M. Dalmonte, G. Pupillo, and P. Zoller, Condensed matter theory of dipolar quantum gases, Chemical Reviews 112, 5012 (2012).
- [5] H. Labuhn, D. Barredo, S. Ravets, S. De Léséleuc, T. Macrì, T. Lahaye, and A. Browaeys, Tunable twodimensional arrays of single rydberg atoms for realizing quantum ising models, Nature 534, 667 (2016).
- [6] J. Zeiher, R. Van Bijnen, P. Schauß, S. Hild, J.-y. Choi, T. Pohl, I. Bloch, and C. Gross, Many-body interferometry of a rydberg-dressed spin lattice, Nature Physics 12, 1095 (2016).
- [7] H. Bernien, S. Schwartz, A. Keesling, H. Levine, A. Omran, H. Pichler, S. Choi, A. S. Zibrov, M. Endres, M. Greiner, et al., Probing many-body dynamics on a 51-atom quantum simulator, Nature 551, 579 (2017).
- [8] J. Hirsch, Charge-density-wave to spin-density-wave transition in the extended hubbard model, Physical Review Letters 53, 2327 (1984).
- [9] H. Lin and J. Hirsch, Condensation transition in the onedimensional extended hubbard model, Physical Review B 33, 8155 (1986).
- [10] R. Micnas, J. Ranninger, S. Robaszkiewicz, and S. Tabor, Superconductivity in a narrow-band system with intersite electron pairing in two dimensions: A mean-field study, Physical Review B 37, 9410 (1988).
- [11] R. Micnas, J. Ranninger, and S. Robaszkiewicz, Superconductivity in narrow-band systems with local nonretarded attractive interactions, Reviews of Modern Physics 62, 113 (1990).
- [12] E. Dagotto, J. Riera, Y. Chen, A. Moreo, A. Nazarenko, F. Alcaraz, and F. Ortolani, Superconductivity near phase separation in models of correlated electrons, Physical Review B 49, 3548 (1994).
- [13] B. Chattopadhyay and D. Gaitonde, Phase diagram of the half-filled extended hubbard model in two dimensions, Physical Review B 55, 15364 (1997).
- [14] M. Vojta, R. Hetzel, and R. Noack, Charge-order transition in the extended hubbard model on a two-leg ladder, Physical Review B 60, R8417 (1999).
- [15] R. Pietig, R. Bulla, and S. Blawid, Reentrant charge order transition in the extended hubbard model, Physical Review Letters 82, 4046 (1999).
- [16] M. Vojta, A. Hübsch, and R. Noack, Phase diagram of the quarter-filled extended hubbard model on a two-leg ladder, Physical Review B 63, 045105 (2001).
- [17] A.-T. Hoang and P. Thalmeier, Coherent potential approximation for charge ordering in the extended hubbard-model, Journal of Physics: Condensed Matter 14, 6639 (2002).
- [18] M. Calandra, J. Merino, and R. H. McKenzie, Metal-

- insulator transition and charge ordering in the extended hubbard model at one-quarter filling, Physical Review B **66**, 195102 (2002).
- [19] K. Rościszewski and A. M. Oleś, Charge order in the extended hubbard model, Journal of Physics: Condensed Matter 15, 8363 (2003).
- [20] N.-H. Tong, S.-Q. Shen, and R. Bulla, Charge ordering and phase separation in the infinite dimensional extended hubbard model, Physical Review B—Condensed Matter and Materials Physics 70, 085118 (2004).
- [21] M. Aichhorn, H. G. Evertz, W. von der Linden, and M. Potthoff, Charge ordering in extended hubbard models: Variational cluster approach, Physical Review B 70, 235107 (2004).
- [22] J. Merino, H. Seo, and M. Ogata, Quantum melting of charge order due to frustration in two-dimensional quarter-filled systems, Physical Review B 71, 125111 (2005).
- [23] B. Davoudi and A.-M. Tremblay, Nearest-neighbor repulsion and competing charge and spin order in the extended hubbard model, Physical Review B 74, 035113 (2006).
- [24] J. Merino, Nonlocal coulomb correlations in metals close to a charge order insulator transition, Physical Review Letters 99, 036404 (2007).
- [25] A. Camjayi, K. Haule, V. Dobrosavljević, and G. Kotliar, Coulomb correlations and the wigner–mott transition, Nature Physics 4, 932 (2008).
- [26] S. Fratini and J. Merino, Unconventional metallic conduction in two-dimensional hubbard-wigner lattices, Physical Review B 80, 165110 (2009).
- [27] A. Amaricci, A. Camjayi, K. Haule, G. Kotliar, D. Tanasković, and V. Dobrosavljević, Extended hubbard model: Charge ordering and wigner-mott transition, Physical Review B 82, 155102 (2010).
- [28] J. Merino, A. Ralko, and S. Fratini, Emergent heavy fermion behavior at the wigner-mott transition, Physical Review Letters 111, 126403 (2013).
- [29] T. Ayral, S. Biermann, and P. Werner, Screening and nonlocal correlations in the extended hubbard model from self-consistent combined gw and dynamical mean field theory, Physical Review B 87, 125149 (2013).
- [30] L. Huang, T. Ayral, S. Biermann, and P. Werner, Extended dynamical mean-field study of the hubbard model with long-range interactions, Physical Review B 90, 195114 (2014).
- [31] H. Hafermann, E. G. van Loon, M. I. Katsnelson, A. I. Lichtenstein, and O. Parcollet, Collective charge excitations of strongly correlated electrons, vertex corrections, and gauge invariance, Physical Review B 90, 235105 (2014).
- [32] E. G. Van Loon, A. I. Lichtenstein, M. I. Katsnelson, O. Parcollet, and H. Hafermann, Beyond extended dynamical mean-field theory: Dual boson approach to the two-dimensional extended hubbard model, Physical Review B 90, 235135 (2014).
- [33] H. Terletska, T. Chen, and E. Gull, Charge ordering and correlation effects in the extended hubbard model, Physical Review B 95, 115149 (2017).
- [34] K. Kapcia, S. Robaszkiewicz, M. Capone, and A. Amaricci, Doping-driven metal-insulator transitions and charge orderings in the extended hubbard model, Physi-

- cal Review B 95, 125112 (2017).
- [35] H. Terletska, T. Chen, J. Paki, and E. Gull, Charge ordering and nonlocal correlations in the doped extended hubbard model, Physical Review B 97, 115117 (2018).
- [36] F. Mivehvar, F. Piazza, T. Donner, and H. Ritsch, Cavity qed with quantum gases: new paradigms in many-body physics, Advances in Physics 70, 1 (2021).
- [37] K. Baumann, C. Guerlin, F. Brennecke, and T. Esslinger, Dicke quantum phase transition with a superfluid gas in an optical cavity, Nature 464, 1301 (2010).
- [38] K. Baumann, R. Mottl, F. Brennecke, and T. Esslinger, Exploring symmetry breaking at the dicke quantum phase transition, Physical Review Letters 107, 140402 (2011).
- [39] R. Mottl, F. Brennecke, K. Baumann, R. Landig, T. Donner, and T. Esslinger, Roton-type mode softening in a quantum gas with cavity-mediated long-range interactions, Science 336, 1570 (2012).
- [40] J. Klinder, H. Keßler, M. Wolke, L. Mathey, and A. Hemmerich, Dynamical phase transition in the open dicke model, Proceedings of the National Academy of Sciences 112, 3290 (2015).
- [41] R. Landig, F. Brennecke, R. Mottl, T. Donner, and T. Esslinger, Measuring the dynamic structure factor of a quantum gas undergoing a structural phase transition, Nature Communications 6, 7046 (2015).
- [42] K. Roux, H. Konishi, V. Helson, and J.-P. Brantut, Strongly correlated fermions strongly coupled to light, Nature Communications 11, 2974 (2020).
- [43] K. Roux, V. Helson, H. Konishi, and J.-P. Brantut, Cavity-assisted preparation and detection of a unitary fermi gas, New Journal of Physics 23, 043029 (2021).
- [44] H. Konishi, K. Roux, V. Helson, and J.-P. Brantut, Universal pair polaritons in a strongly interacting fermi gas, Nature 596, 509 (2021).
- [45] X. Zhang, Y. Chen, Z. Wu, J. Wang, J. Fan, S. Deng, and H. Wu, Observation of a superradiant quantum phase transition in an intracavity degenerate fermi gas, Science 373, 1359 (2021).
- [46] V. Helson, T. Zwettler, F. Mivehvar, E. Colella, K. Roux, H. Konishi, H. Ritsch, and J.-P. Brantut, Density-wave ordering in a unitary fermi gas with photon-mediated interactions, Nature 618, 716 (2023).
- [47] T. Zwettler, G. Del Pace, F. Marijanovic, S. Chattopadhyay, T. Bühler, C.-M. Halati, L. Skolc, L. Tolle, V. Helson, G. Bolognini, et al., Nonequilibrium dynamics of long-range interacting fermions, Physical Review X 15, 021089 (2025).
- [48] T. Bühler, A. Fabre, G. Bolognini, Z. Xue, T. Zwettler, G. Del Pace, and J.-P. Brantut, Microscopy of cavityinduced density-wave ordering in ultracold gases, arXiv preprint arXiv:2511.08510 (2025).
- [49] J. Keeling, M. Bhaseen, and B. Simons, Fermionic superradiance in a transversely pumped optical cavity, Physical Review Letters 112, 143002 (2014).
- [50] F. Piazza and P. Strack, Umklapp superradiance with a collisionless quantum degenerate fermi gas, Physical Review Letters 112, 143003 (2014).
- [51] Y. Chen, Z. Yu, and H. Zhai, Superradiance of degenerate fermi gases in a cavity, Physical Review Letters 112, 143004 (2014).
- [52] W. Hofstetter and T. Qin, Quantum simulation of strongly correlated condensed matter systems, Journal of Physics B: Atomic, Molecular and Optical Physics 51,

- 082001 (2018).
- [53] Y. Li, L. He, and W. Hofstetter, Lattice-supersolid phase of strongly correlated bosons in an optical cavity, Physical Review A 87, 051604 (2013).
- [54] N. Dogra, F. Brennecke, S. D. Huber, and T. Donner, Phase transitions in a bose-hubbard model with cavitymediated global-range interactions, Physical Review A 94, 023632 (2016).
- [55] A. E. Niederle, G. Morigi, and H. Rieger, Ultracold bosons with cavity-mediated long-range interactions: A local mean-field analysis of the phase diagram, Physical Review A 94, 033607 (2016).
- [56] J. Panas, A. Kauch, and K. Byczuk, Spectral properties and phase diagram of correlated lattice bosons in an optical cavity within bosonic dynamical mean-field theory, Physical Review B 95, 115105 (2017).
- [57] L. Carl, R. Rosa-Medina, S. D. Huber, T. Esslinger, N. Dogra, and T. Dubcek, Phases, instabilities and excitations in a two-component lattice model with photonmediated interactions, Physical Review Research 5, L032003 (2023).
- [58] J. Klinder, H. Keßler, M. R. Bakhtiari, M. Thorwart, and A. Hemmerich, Observation of a superradiant mott insulator in the dicke-hubbard model, Physical Review Letters 115, 230403 (2015).
- [59] R. Landig, L. Hruby, N. Dogra, M. Landini, R. Mottl, T. Donner, and T. Esslinger, Quantum phases from competing short-and long-range interactions in an optical lattice, Nature 532, 476 (2016).
- [60] L. Hruby, N. Dogra, M. Landini, T. Donner, and T. Esslinger, Metastability and avalanche dynamics in strongly correlated gases with long-range interactions, Proceedings of the National Academy of Sciences 115, 3279 (2018).
- [61] A. Camacho-Guardian, R. Paredes, and S. F. Caballero-Benítez, Quantum simulation of competing orders with fermions in quantum optical lattices, Physical Review A 96, 051602 (2017).
- [62] L. Tolle, A. Sheikhan, T. Giamarchi, C. Kollath, and C.-M. Halati, Fluctuation-induced bistability of fermionic atoms coupled to a dissipative cavity, Physical Review Letters 134, 133602 (2025).
- [63] L. Tolle, A. Sheikhan, T. Giamarchi, C. Kollath, and C.-M. Halati, Steady state diagram of interacting fermionic atoms coupled to dissipative cavities, arXiv preprint arXiv:2509.07469 (2025).
- [64] F. Piazza, P. Strack, and W. Zwerger, Bose–einstein condensation versus dicke–hepp–lieb transition in an optical cavity, Annals of Physics 339, 135 (2013).
- [65] M. Snoek, I. Titvinidze, C. Tőke, K. Byczuk, and W. Hofstetter, Antiferromagnetic order of strongly interacting fermions in a trap: real-space dynamical mean-field analysis, New Journal of Physics 10, 093008 (2008).
- [66] C. Maschler and H. Ritsch, Cold atom dynamics in a quantum optical lattice potential, Physical Review Letters 95, 260401 (2005).
- [67] C. Maschler, I. B. Mekhov, and H. Ritsch, Ultracold atoms in optical lattices generated by quantized light fields, The European Physical Journal D 46, 545 (2008).
- [68] D. Jaksch, C. Bruder, J. I. Cirac, C. W. Gardiner, and P. Zoller, Cold bosonic atoms in optical lattices, Physical Review Letters 81, 3108 (1998).
- [69] W. Zwerger, Mott-hubbard transition of cold atoms in optical lattices, Journal of Optics B: Quantum and Semi-

- classical Optics 5, S9 (2003).
- [70] I. Bloch, J. Dalibard, and W. Zwerger, Many-body physics with ultracold gases, Reviews of Modern Physics 80, 885 (2008).
- [71] A. Hoffmann and A. Pelster, Visibility of cold atomic gases in optical lattices for finite temperatures, Physical Review A 79, 053623 (2009).
- [72] S. Giorgini, L. P. Pitaevskii, and S. Stringari, Theory of ultracold atomic fermi gases, Reviews of Modern Physics 80, 1215 (2008).
- [73] F. Piazza and P. Strack, Quantum kinetics of ultracold fermions coupled to an optical resonator, Physical Review A 90, 043823 (2014).
- [74] A. Georges, G. Kotliar, W. Krauth, and M. J. Rozenberg, Dynamical mean-field theory of strongly correlated fermion systems and the limit of infinite dimensions, Reviews of Modern Physics 68, 13 (1996).
- [75] R. Helmes, T. Costi, and A. Rosch, Mott transition of fermionic atoms in a three-dimensional optical trap, Physical Review Letters 100, 056403 (2008).
- [76] A. Sotnikov, Critical entropies and magnetic-phase-

- diagram analysis of ultracold three-component fermionic mixtures in optical lattices, Physical Review A 92, 023633 (2015).
- [77] P. Kumar, T. Mertz, and W. Hofstetter, Interactioninduced topological and magnetic phases in the hofstadter-hubbard model, Physical Review B 94, 115161 (2016).
- [78] J. Merino and R. H. McKenzie, Superconductivity mediated by charge fluctuations in layered molecular crystals, Physical Review Letters 87, 237002 (2001).
- [79] R. H. McKenzie, J. Merino, J. Marston, and O. Sushkov, Charge ordering and antiferromagnetic exchange in layered molecular crystals of the θ type, Physical Review B **64**, 085109 (2001).
- [80] H. Park, K. Haule, and G. Kotliar, Cluster dynamical mean field theory of the mott transition, Physical Review Letters 101, 186403 (2008).
- [81] A. Geißler, Lattice-supersolids in bosonic quantum gases with Rydberg excitations, Ph.D. thesis, Universitätsbibliothek Johann Christian Senckenberg (2018).